The Astrophysical Journal, 916:112 (15pp), 2021 August 1 https://doi.org/10.3847/1538-4357/ac04b5

Dynamical Model of the Milky Way Using APOGEE and Gaia Data

Maria Selina Nitschai[1], Anna-Christina Eilers[2,4], Nadine Neumayer[1], Michele Cappellari[3], and Hans-Walter Rix[1]
[1] Max Planck Institute for Astronomy, Königstuhl 17, D-69117 Heidelberg, Germany; nitschai@mpia.de
[2] MIT Kavli Institute for Astrophysics and Space Research, 77 Massachusetts Avenue, Cambridge, MA 02139, USA
[3] Sub-department of Astrophysics, Department of Physics, University of Oxford, Denys Wilkinson Building, Keble Road, Oxford OX1 3RH, UK
Received 2021 January 26; revised 2021 May 19; accepted 2021 May 20; published 2021 August 4

Abstract

We construct a dynamical model of the Milky Way disk from a data set that combines Gaia EDR3 and APOGEE data throughout galactocentric radii in the range 5.0 kpc $\leqslant R \leqslant$ 19.5 kpc. We make use of the spherically aligned Jeans anisotropic method to model the stellar velocities and their velocity dispersions. Building upon our previous work, our model is now fitted to kinematic maps that have been extended to larger galactocentric radii due to the expansion of our data set, probing the outer regions of the Galactic disk. Our best-fitting dynamical model suggests a logarithmic density slope of $\alpha_{\rm DM} = -1.602 \pm 0.079_{\rm syst}$ for the dark matter halo and a dark matter density of $\rho_{\rm DM}(R_\odot) = (8.92 \pm 0.56_{\rm syst}) \times 10^{-3}\, M_\odot\,{\rm pc}^{-3}$ $(0.339 \pm 0.022_{\rm syst}\,{\rm GeV\,cm}^3)$. We estimate a circular velocity at the solar radius of $v_{\rm circ} = (234.7 \pm 1.7_{\rm syst})$ km s^{-1} with a decline toward larger radii. The total mass density is $\rho_{\rm tot}(R_\odot) = (0.0672 \pm 0.0015_{\rm syst})\, M_\odot\,{\rm pc}^{-3}$ with a slope of $\alpha_{\rm tot} = -2.367 \pm 0.047_{\rm syst}$ for 5 kpc $\leqslant R \leqslant$ 19.5 kpc, and the total surface density is $\Sigma(R_\odot,\ |z| \leqslant 1.1\ {\rm kpc}) = (55.5 \pm 1.7_{\rm syst})\, M_\odot\,{\rm pc}^{-2}$. While the statistical errors are small, the error budget of the derived quantities is dominated by the three to seven times larger systematic uncertainties. These values are consistent with our previous determination, but the systematic uncertainties are reduced due to the extended data set covering a larger spatial extent of the Milky Way disk. Furthermore, we test the influence of nonaxisymmetric features on our resulting model and analyze how a flaring disk model would change our findings.

Unified Astronomy Thesaurus concepts: Milky Way dynamics (1051); Milky Way disk (1050)

Supporting material: tar.gz file

1. Introduction

Dynamical models are important for our understanding of galaxies. They describe the distribution of stars over orbits in a gravitational potential (Binney & Tremaine 1987). Hence, we can describe a galaxy as stars orbiting in a smooth gravitational potential by interpreting the combined stellar position and velocity information (e.g., Syer & Tremaine 1996; Rix et al. 1997; Cappellari 2008; Binney & McMillan 2011). This allows us to infer the gravitational potential, circular velocity curve, mass distribution, and dark matter density of a galaxy (e.g., Rix & Bovy 2013).

For most external galaxies, dynamical models usually suffer from degeneracies due to limited data. Since only line-of-sight observations are available, the data cannot provide the three-dimensional information that is needed to fully constrain dynamical models. There are only a very few cases where the full velocity information is available, and they usually have a limited quality of data (e.g., van de Ven et al. 2006; Watkins et al. 2015). However, our own Galaxy can be observed in great detail with high-precision measurements from various stellar surveys. In the past several years, there has been a plethora of surveys for the Milky Way, such as APOGEE (Allende Prieto et al. 2008; Majewski et al. 2017) and Gaia (Gaia Collaboration et al. 2016), providing astrometric and spectroscopic information for a large sample of stars.

Many different dynamical models can be found in the literature (see Rix & Bovy 2013), such as Jeans modeling (e.g., Cappellari 2008; Bovy & Tremaine 2012; Zhang et al. 2013), action-based models (e.g., Binney & McMillan 2011; Binney 2012; Bovy & Rix 2013), Schwarzschild models (e.g., Rix et al. 1997; van der Marel et al. 1998; Gebhardt et al. 2000; Cappellari et al. 2006; van den Bosch et al. 2008), and made-to-measure models (e.g., Syer & Tremaine 1996; de Lorenzi et al. 2009; Dehnen 2009; Wegg et al. 2015; Portail et al. 2017). For this paper, we will use the Jeans modeling approach. Jeans models are based on the Jeans equations (Jeans 1915, 1922), which are derived from the steady-state Boltzmann equation under the assumption of axisymmetry. The steady-state collisionless Boltzmann equation needs to be satisfied by the distribution function of the system, which describes the position and velocity of the stars in equilibrium and steady state under the gravitational influence of a smooth potential (Binney & Tremaine 1987). The solutions of the Jeans equations describe the moments of the velocity distribution and the density of a collection of stars in a gravitational potential. However, to obtain a unique solution, one has to assume the shape and orientation of the velocity ellipsoid. Cappellari (2008) reviewed the possible natural choices for this alignment, which are prolate spheroidal coordinates, spherical coordinates, and cylindrical ones.

Previously, we used the Gaia Data Release 2 (DR2) kinematics to construct an axisymmetric dynamical model of the Milky Way disk (Nitschai et al. 2020, hereafter Paper I). There we used the new spherically aligned Jeans anisotropic modeling (JAM$_{\rm sph}$; Cappellari 2020) method, since the Gaia data (Everall et al. 2019; Hagen et al. 2019) showed that the velocity ellipsoid is closer to being spherically aligned than

[4] NASA Hubble Fellow.

cylindrically (JAM_{cyl}; Cappellari 2008). But we also compared the results against JAM_{cyl} and found negligible differences.

The known deviations from equilibrium and axisymmetry for the Milky Way (Widrow et al. 2012; Antoja et al. 2018; Gaia Collaboration et al. 2018a), which are in conflict with our model assumptions, are not uncommon for other galaxies too, but models are still able to recover the average kinematic properties (Cappellari et al. 2013), even from less precise data. In the case of the JAM method, it has been used to model integral-field stellar kinematics of large numbers of external galaxies (Cappellari 2016). It has been tested against *N*-body simulations (Lablanche et al. 2012; Li et al. 2016) and in real galaxies against CO circular velocities (Leung et al. 2018), including barred and non-perfectly axisymmetric galaxies similar to the Milky Way. In both cases, it recovers unbiased density profiles even more accurately than the Schwarzschild (Schwarzschild 1979) approach (Leung et al. 2018), which was also confirmed (Jin et al. 2019) by using Illustris cosmological *N*-body simulations (Vogelsberger et al. 2014). Hence, we expect that JAM will be able to capture the main kinematic features of the Milky Way and give accurate results for the total density and circular velocity, even more since we use the spherical alignment, JAM_{sph}.

In this paper, we build upon Paper I by extending the maximal galactocentric radius of the data from ∼12 to ∼20 kpc. This allows us to extend our model to the outer parts of the Galactic disk and better constrain the model parameters. Furthermore, we improve our model by including the uncertainties of the kinematic maps at each position. The extended data set also allows us to test our model when using a flared outer disk, as suggested by, e.g., Gyuk et al. (1999), Momany et al. (2006), López-Corredoira & Molgó (2014), and Li et al. (2019).

The outline of this paper is as follows. We describe the data set and derived kinematic maps with their uncertainties in Section 2. In Section 3, we describe the components of our mass model for the Galaxy and our modeling method. In the end, we show our results for this extended data set and the investigation into the effect of the nonaxisymmetries in Section 4, and we also show the results for a model with a flared disk. Finally, in Section 5, we summarize our results. In Appendices B and C, we include further tests for our model.

2. Data

In this paper, we combine two data sets, one of the giant stars from the Gaia early data release 3 (EDR3) with radial velocities (Gaia Collaboration et al. 2021) and one of the red giant branch (RGB) stars from APOGEE and Gaia (Hogg et al. 2019). This combined data set will allow us to reach out to large galactocentric radii.

2.1. Data Set

Gaia provides precise parallax information locally, but further away from the Sun, the distance uncertainties dominate. In addition, it is known that there is an parallax offset in Gaia DR2 (Lindegren et al. 2018; Zinn et al. 2019; Schönrich et al. 2019), and a parallax bias has also been discovered in Gaia EDR3 (Lindegren et al. 2021a). There has been an attempt to map the dependencies of the parallax bias, but since the dependencies are nontrivial, it is not possible to have a definitive correction (Lindegren et al. 2021b).

In this work, we update the data from Paper I using Gaia EDR3 (Gaia Collaboration et al. 2021). The important update for our study is the higher precision in the astrometry in EDR3; however, the radial velocities have not been updated and have been adopted from DR2. In addition, EDR3 does not have extinction or reddening values; hence, we crossmatched EDR3 with DR2 using the given crossmatch catalog by Torra et al. (2021) in order to get these values. For distances, we use the photogeometric distance estimates by Bailer-Jones et al. (2021) for the Gaia EDR3 in order to avoid the parallax bias and high uncertainties further away from the Sun.

The selection criteria we apply are the same as in Paper I. Since giant stars are the main contribution in Gaia at distances larger than 1 kpc from the Sun and can be measured out to large distances due to their brightness, we select only them in this subsample. They are selected based on their absolute magnitude, $M_G = m_G - 5 \cdot \log d + 5 - A < 3.9$, given the extinction by Gaia DR2 and d being the distance from Bailer-Jones et al. (2021), their intrinsic color $(G_{BP} - G_{RP})_0 > 0.95$, with the reddening taken from Gaia DR2 and parallaxes with relative uncertainty $\varpi/\epsilon_\varpi > 5$.

These data are precise only around the Sun and not far beyond.

In order to probe larger galactocentric distances, Hogg et al. (2019) obtained precise spectrophotometric distance estimates for 44,784 red giant stars with a data-driven model. They combined spectroscopic data from APOGEE (Majewski et al. 2017) DR14 (Abolfathi et al. 2018) with photometric information from Gaia (Gaia Collaboration et al. 2016) DR2 (Gaia Collaboration et al. 2018b), the Two Micron All Sky Survey (2MASS; Skrutskie et al. 2006), and the Wide-field Infrared Survey Explorer (WISE; Wright et al. 2010). These data allow us to probe larger distances, out to Galactic radii of ∼20 kpc, than with Gaia data alone.

These RGB stars were selected with a cut at $\log g < 2.2$, in order to have stars more luminous than the red clump. For more details on the quality cuts for these stars, see Hogg et al. (2019).

In order to extend our data set to larger galactocentric radii, we combine the data set based on Gaia EDR3 with that from Hogg et al. (2019). For the combined data set, we require that the proper motion and line-of-sight velocities of all stars are finite and in the area of $-30° < \phi < 30°$. For sources that are in both data sets, we prefer the values from Hogg et al. (2019) for our further calculations.

The remaining stars from the Hogg et al. (2019) data are 34,180 and 2,823,509 stars that are only in Gaia. In total, we have 2,857,689 stars that will be used in the further analysis.

2.2. Kinematic Maps

In order to calculate the kinematic maps of the Milky Way, we transform the positions and velocities of the stars in our combined data set into a galactocentric reference frame.

We assume $R_\odot = 8.178$ kpc as the distance to the Galactic center (Gravity Collaboration et al. 2019), a vertical displacement of the Sun from the midplane of $z_\odot = 0.02$ kpc (Joshi 2007), and $(U_\odot, V_\odot, W_\odot) = (-11.1, 247.4, 7.2)$ km s^{-1} as solar velocities in cylindrical Galactic coordinates (from Schönrich et al. 2010; Gravity Collaboration et al. 2019; Reid et al. 2009, respectively). We require the data to have $|z| \leqslant 7$ kpc because we have more stars toward positive z values, which are not covering the whole area and creating gaps in our data. Hence, in order to avoid an asymmetric and discontinuous data set, we

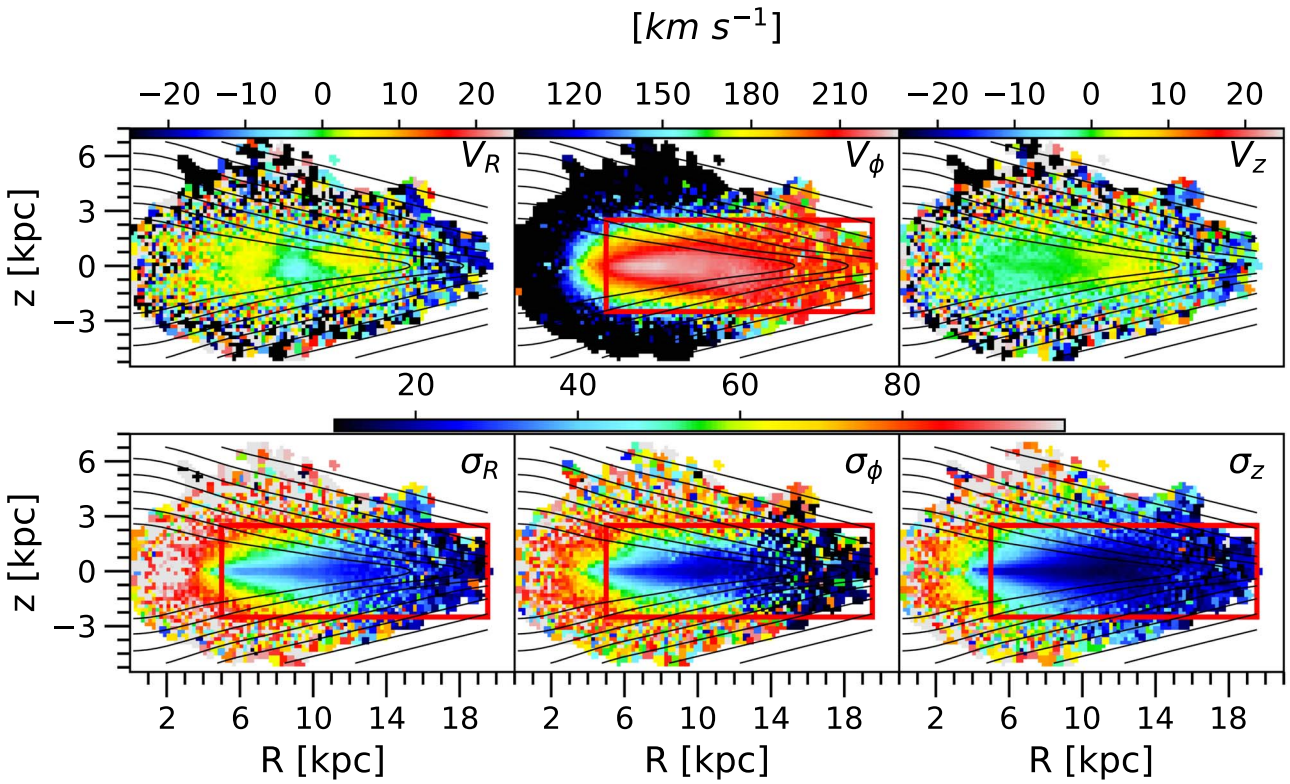

Figure 1. Velocity maps for the combined data from Gaia EDR3 with that from Hogg et al. (2019). The colors represent the mean velocity or dispersion of the Voronoi bins, as described in Section 2.2. The top panels show the velocities, and the bottom panels show the velocity dispersions. From left to right are the velocities and velocity dispersions in R, ϕ, and z. All color maps are in kilometers per second. Inside the red boxes are the data that we will actually use for the JAM model, and the black lines are the stellar density (as described in Section 3.1.1) contours.

exclude stars with too-high z values from the beginning. The stars that are excluded would not be considered in our further analysis anyway, since they are halo stars and lie outside of the disk region we want to model. We then divide our data into 200 pc × 200 pc cells and do Voronoi binning using the VORBIN package[5] (Cappellari & Copin 2003), requiring a minimum of five stars for each Voronoi bin. We use the Voronoi binning on our already divided into 200 pc × 200 pc data to fully make use of the data, especially toward larger radii and z, where the stars are not as dense and we would not get more than five stars in a cell. With this method, we can combine the data from cells without enough stars in them but still keep as the smallest bin the 200 pc × 200 pc cell in the central region of our kinematic maps around the solar position, where we have numerous stars. For each bin, we calculate the mean and standard deviation of the velocities. The final number of bins is 2899 and covers a volume with extreme cylindrical coordinates of $0.18\,\mathrm{kpc} \leqslant R \leqslant 19.5\,\mathrm{kpc}$ and $-5.02\,\mathrm{kpc} \leqslant z \leqslant 6.8\,\mathrm{kpc}$.

The created velocity maps of the combined data set in cylindrical coordinates are shown in Figure 1. As expected, the stars around the solar position extend to larger galactocentric heights z than at larger or smaller radii. However, thanks to the Voronoi binning, we get a continuous covered area up to a radius of 19.5 kpc without any gaps in the kinematics.

The selection function of Gaia DR2 (Boubert et al. 2020; Boubert & Everall 2020) and specifically of the radial velocity sample (Rybizki et al. 2021), since we only select stars in EDR3 that have radial velocities in DR2 and for APOGEE (Bovy et al. 2014; Mackereth & Bovy 2020) will not affect our model significantly, since we study the kinematics of the observed stars, at a given position. The stellar tracer density is assumed, not fitted, and the selection function at a given position does not depend strongly on the velocities of the objects.

To find the uncertainties for our kinematic maps, we choose to use the bootstrapping method (e.g., Efron & Tibshirani 1993). We selected this method and not error propagation because it provides a more robust estimate of the uncertainties. The propagated uncertainties from radial velocities and proper-motion measurements tend to underestimate the true uncertainties. In detail, we draw 100 random samples of stars with their velocities and redo the Voronoi binning, again calculating the mean velocity and velocity dispersion for each bin for each of the samples. Afterward, we find the uncertainties of the bin by calculating the standard deviation of the 100 mean velocities and velocity dispersions.

The uncertainty maps are shown in Figure 2. Errors around the Sun and the midplane are much smaller ($\leqslant 4\,\mathrm{km\,s^{-1}}$) than at larger heliocentric distances because there are more stars detected and their measurements are more precise, since they are closer to us.

The uncertainties are also higher toward the Galactic center. In this area, starting at 5 kpc, the bar dominates the kinematics (Wegg et al. 2015; Bovy et al. 2019) and hence would break the axisymmetry assumptions of our model. To avoid that, we exclude data with $R < 5\,\mathrm{kpc}$. Additionally, we also exclude stars with $|z| \geqslant 2.5\,\mathrm{kpc}$, which is the same range we had in Paper I, in order to exclude halo stars. Similar to Paper I, we ignore the halo distribution, since it is not well known, and in this regime, we expect to mainly have disk stars. The red boxes in Figures 1 and 2 show the area we will investigate, and they

[5] We use Python version 3.1.4 of the VORBIN package, available from https://pypi.org/project/vorbin/.

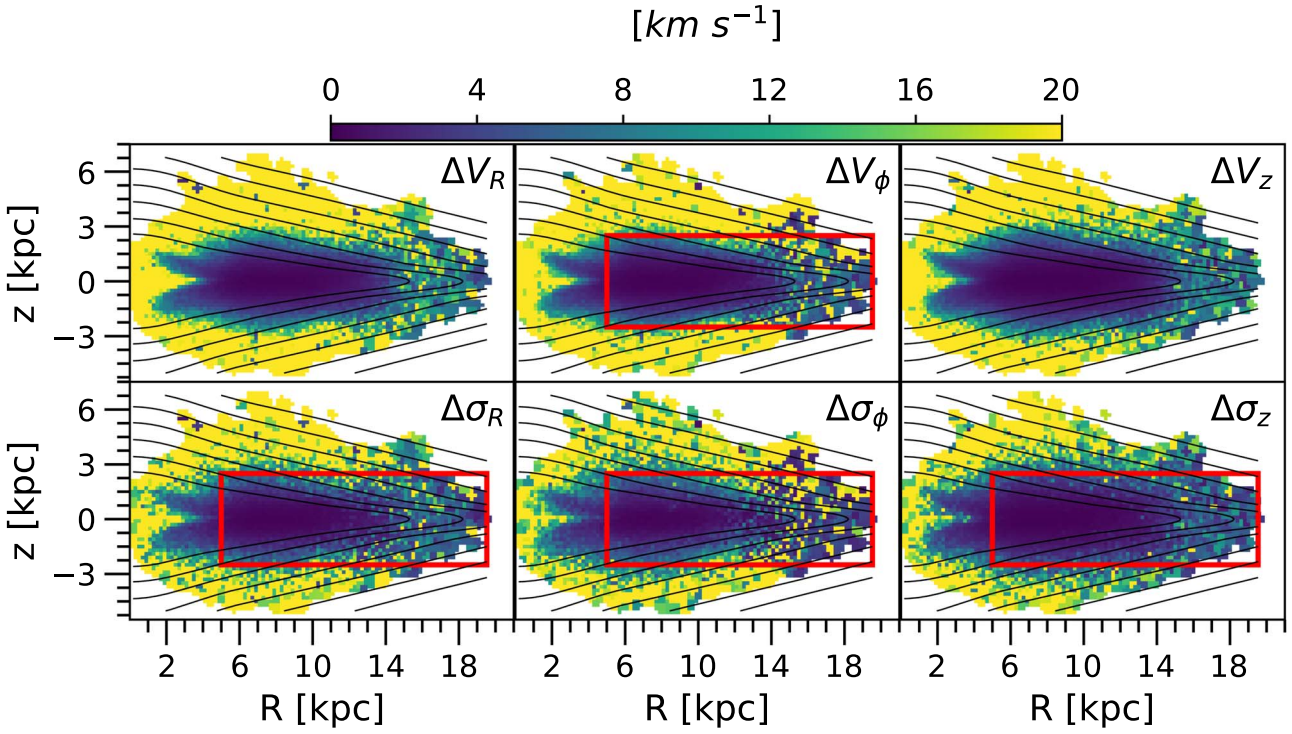

Figure 2. Uncertainty maps for the combined data. Similar to Figure 1, the colors represent the uncertainty value for each Voronoi bin. The top panels show the velocities, and the bottom panels show the velocity dispersions. From left to right are the velocities and velocity dispersions in R, ϕ, and z. Inside the red boxes are the errors that we will use in calculating the χ^2 of our JAM model, and the black lines are the stellar density (Section 3.1.1) contours.

have 1404 bins; the data outside the boxes are excluded from further analysis.

3. Methods

3.1. Mass Distribution of the Milky Way Model

To construct a dynamical model, we need an estimate of the tracer distribution and mass density of the Galaxy. We will assume the same model for the Milky Way as in Paper I; a detailed description and explanation can be found there, and we give a brief summary in this section. In addition to this model, we also investigate a model with a flaring disk in Section 3.1.2.

3.1.1. Distribution with an Exponential Disk Model

Our main stellar model makes use of the Jurić et al. (2008) disk stellar distribution, normalized to the local luminosity density from Flynn et al. (2006). However, we ignore the stellar halo component because in the area we are probing with our data set, the stellar mass distribution is dominated by the disk component.

The disk is decomposed into a sum of two exponential components, the thin and thick disk, with different scale lengths $(L_{\rm thin}, L_{\rm thick}) = (2.6, 3.6)$ kpc and heights $(H_{\rm thin}, H_{\rm thick}) = (0.3, 0.9)$ kpc (Jurić et al. 2008):

$$\rho_{\rm D}(R, z, L, H) = \rho(R_\odot, 0)\exp\left(-\frac{R - R_\odot}{L} - \frac{|z|}{H}\right), \quad (1)$$

$$\rho_{\rm D}(R, z) = \rho_{\rm D}(R, z, L_{\rm thin}, H_{\rm thin}) + f \cdot \rho_{\rm D}(R, z, L_{\rm thick}, H_{\rm thick}), \quad (2)$$

where $f = 0.12$ is the thick disk normalization relative to the thin disk (Jurić et al. 2008). In addition, we combined that with an axisymmetric bulge (McMillan 2017; Bissantz & Gerhard 2002).

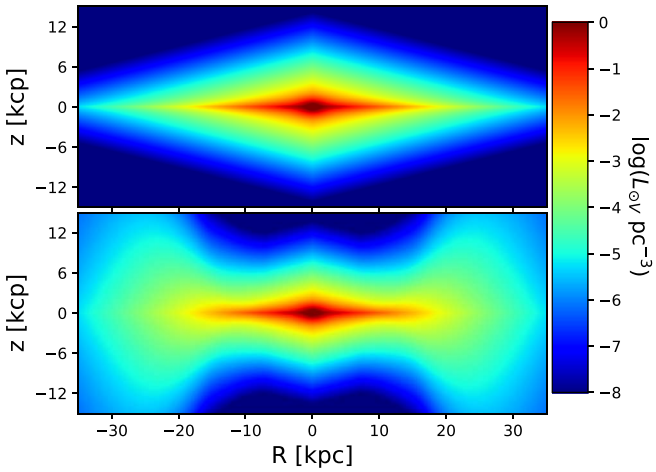

Figure 3. Luminosity density profile of the Milky Way without and with flaring. The top panel shows the stellar luminosity density for our main model described in Section 3.1.1. The bottom panel shows the flared Milky Way model (see Section 3.1.2). The x-axis is the radial direction, R, reaching up to ±35 kpc away from the Galactic center at (0, 0) kpc, and the y-axis is the displacement from the midplane, z, ranging up to ±15 kpc. The color map is the logarithmic luminosity density.

The luminosity density profile of this model is shown in the top panel of Figure 3.

We approximate this stellar model with a multi-Gaussian expansion (MGE; Emsellem et al. 1994; Cappellari 2002) using the MGE fitting method (Cappellari 2002) and MGEFIT software package,[6] which is necessary in order to apply the JAM model (Cappellari 2008, 2020).

[6] We use Python version 5.0.12 of the MGEFIT package, available from https://pypi.org/project/mgefit/.

For the mass density of the Galaxy, we need to include the gas and dark matter contribution. For the gas component, we add the H_2 and H_{II} distribution from McMillan (2017). For simplicity, we ignore the hole in the center of the density profile, since the hole is outside of the range we are probing. In Paper I, we showed that this does not change the dynamical model significantly. Like for the stellar model, we use the MGEFIT package (Cappellari 2002) to fit the created image of the gas density. This MGE will be added to the potential density and be kept fixed during the model fit to the quoted mass by McMillan (2017).

As a dark matter halo, we assume a generalized Navarro–Frenk–White profile (gNFW; Wyithe et al. 2001),

$$\rho_{\rm DM} = \rho_s \left(\frac{m}{r_s}\right)^{\alpha_{\rm DM}} \left(\frac{1}{2} + \frac{1}{2}\frac{m}{r_s}\right)^{-3-\alpha_{\rm DM}}, \quad (3)$$

where

$$m^2 = R^2 + (z/q_{\rm DM})^2, \quad (4)$$

r_s the scale radius, $\alpha_{\rm DM}$ is the dark matter slope, and $q_{\rm DM}$ is the axial ratio. If $\alpha_{\rm DM} = -1$, the profile represents the classical NFW dark matter profile (Navarro et al. 1996).

The dark matter profile is a one-dimensional profile, and we fit this with Gaussians using the MGE_FIT_1D routine from the MGEFIT package. It can be made oblate or prolate for use with the model depending on the value of $q_{\rm DM}$.

The model assumptions cause systematic uncertainties that strongly depend on the values we choose for the different parameters but also the model itself. We tested the effects of the disk parameters in Paper I for the circular velocity and total density in order to get an understanding of these uncertainties.

3.1.2. Distribution with a Flared Disk Model

We know that the outer part of our Galaxy, beyond 15 kpc, is warped and flared, but the details of its shape are still uncertain (Bland-Hawthorn & Gerhard 2016). These structures were first detected in the gas component of the disk (Kerr 1957; Oort et al. 1958; Grabelsky et al. 1987; May et al. 1997) but can also be detected in the three-dimensional distribution of stars (e.g., Liu et al. 2017; Anders et al. 2019; Skowron et al. 2019).

A flared disk means that the vertical scale height grows with increasing radius. The stellar flare in the outer Galactic disk has been observed and the scale height modeled as a function of the radius by many studies for the outer disk (e.g., Gyuk et al. 1999; Alard 2000; López-Corredoira et al. 2002; Yusifov 2004; Momany et al. 2006; Reylé et al. 2009; López-Corredoira & Molgó 2014; Li et al. 2019).

Since we are probing a large range of Galactic radii up to ∼20 kpc, our data extend to the regime where the flare is visible. Hence, in addition to our main exponential model described in the previous subsection, we investigate how a flared disk would change our results.

Even though there are many studies of the flare, there is no single parameterization for it. We decided to base the flare we use on the work of López-Corredoira & Molgó (2014), because they give a parameterization for the scale height for the thin and thick disk. In detail, we keep the density profile the same as for our main model and only modify the scale heights, $H_{\rm thin}$, $H_{\rm thick}$, for larger radii,

$$H_{\rm thin} = H_{\rm thin}(R_\odot)\left[1 + \sum_{i=1}^{2} k_{i,\rm thin}(R - R_\odot)^i\right], R > R_\odot, \quad (5)$$

$$H_{\rm thick} = H_{\rm thick}(R_{\rm ft})\left[1 + \sum_{i=1}^{2} k_{i,\rm thick}(R - R_{\rm ft})^i\right], R > R_{\rm ft}, \quad (6)$$

with $k_{i,\rm thin} = (-0.037\ \mathrm{kpc}^{-1}, 0.052\,\mathrm{kpc}^{-2})$, $k_{i,\rm thick} = (0.021\ \mathrm{kpc}^{-1}, 0.006\,\mathrm{kpc}^{-2})$, and $R_{\rm ft} = 6.9$ kpc (López-Corredoira & Molgó 2014).

Since the flare starts only at larger radii, we assume the scale height for the thin disk to also be constant up to the solar position. For $R < R_\odot$, $H_{\rm thin} = H_{\rm thin}(R_\odot)$, and for $R < R_{\rm ft}$, $H_{\rm thick} = H_{\rm thick}(R_{\rm ft})$. As values for the scale heights at the solar position, we use the values from Jurić et al. (2008), $H_{\rm thin}(R_\odot) = 300$ pc and $H_{\rm thick}(R_\odot) = 900$ pc. See the bottom panel of Figure 3 for the density profile with the flare.

3.2. MGE with Negative Gaussians but Nonnegative Density Everywhere

An MGE with only positive Gaussians cannot describe a density distribution like the one in Figure 3. A good fit can be obtained for a restricted spatial extent, allowing for negative Gaussians (keyword `negative = True` in MGE_FIT_SECTORS of the MGEFIT package of Cappellari 2002). However, we verified that in this case, the resulting MGE has a strongly negative density at larger radii and produces clearly nonphysical results when used with JAM. The inability to constrain the density to be positive and the need to test for the positivity of the total density are general problems when allowing for a negative Gaussian in MGE fits.

To obtain an acceptable MGE fit to the flared disk while guaranteeing a positive total density, we needed to make some modifications to the MGE_FIT_SECTORS procedure. For this, in addition to the usual positive Gaussian basis functions in the MGE, we introduced a set of new basis functions, which we produced by coadding four positive and negative Gaussians with the same absolute peak value in such a way that their sum is everywhere positive, as follows:

$$G(R, z) = e^{-\frac{1}{2\sigma^2}\left(\frac{R^2}{f^2} + \frac{z^2}{f^2 q^2}\right)} + e^{-\frac{1}{2\sigma^2}\left(R^2 + \frac{z^2}{q^2}\right)} - e^{-\frac{1}{2\sigma^2}\left(\frac{R^2}{f^2} + \frac{z^2}{q^2}\right)} - e^{-\frac{1}{2\sigma^2}\left(R^2 + \frac{z^2}{f^2 q^2}\right)}. \quad (7)$$

Here σ and q are two parameters that change for different MGE components (like the corresponding parameters for the MGE Gaussians), while $f = 0.9$ is a constant $f \lesssim 1$, which is the same for all basis functions. With this definition, the new MGE basis function is $G(R, z) = 0$ along the R- or z-axis and presents four bisymmetric maxima, as illustrated in Figure 4.

The new basis function $G(R, z)$ has an asymptotic behavior at large radii $G \sim \exp(-r^2)$ for $r \to \infty$, as the standard MGE, while along the axes, $G \sim R^2$ for $R \to 0$ and $G \sim z^2$ for $z \to 0$. This implies that, while it can describe decreasing profiles toward the center, it cannot approximate drops of the central density profile steeper than $\rho \propto r^2$. For this reason, it can only approximate the flared density of Figure 3 down to a certain isophote.

Apart from the introduction of the new basis function, the fit is obtained using the same algorithm described in Cappellari (2002)

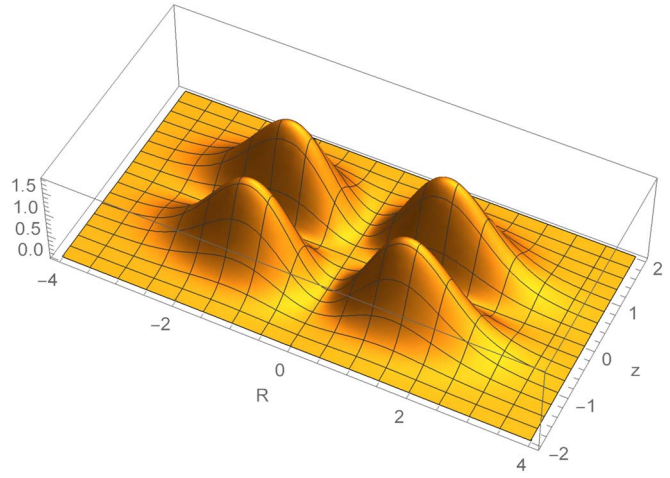

Figure 4. New MGE basis function. This basis function consists of four positive/negative Gaussians centered on the origin. When combined with the usual positive Gaussians, it allows for extra flexibility in the MGE fitting while still guaranteeing a nonnegative density everywhere.

while still enforcing positivity constraints for all basis functions. Once the fit converges, all the four Gaussian basis functions are split into their four individual Gaussian components in output, producing an MGE that is composed of both positive and negative Gaussians. In this way, no further changes are required to use the produced MGE model with other software like JAM.

The new MGE has 49 Gaussians, but these come from 28 basis functions, some of which are constructed from groups of four Gaussians, which are fitted as single basis functions. This new implementation of the MGE fit is/will be included in the new release of the MGE package (footnote 2).

3.3. Modeling

As a dynamical model, we use the $\mathrm{JAM_{sph}}$ approach[7] (Cappellari 2020), which is based on the solution of the axisymmetric Jeans equations and assumes a spherically aligned velocity ellipsoid (Bacon et al. 1983; Bacon 1985). The spherical alignment has proven to describe the Gaia data in the outer halo (Wegg et al. 2019) and in the disk region (Hagen et al. 2019; Everall et al. 2019). This was also confirmed by the results in Paper I.

In Figure 1, we have drawn a red square around the data we will use for our model; we only fit the axisymmetric in-plane kinematics (v_ϕ, σ_r, σ_ϕ, σ_z). Neither vertical motion nor tracer distribution are fit. Due to the steady-state assumption of our model, v_R and v_z are assumed to be zero, and therefore they do not need to be fitted. The deviations from zero in the data due to nonaxisymmetric signatures (Antoja et al. 2018; Gaia Collaboration et al. 2018a) are small enough for the purposes of our model.

The features we do not include in our stellar distribution of the Galaxy are the bar in the inner region and the warp in the outer disk, since both signatures are nonaxisymmetric and we cannot model them with JAM. In particular, the bar dominates within 5 kpc of the Galactic center (Wegg et al. 2015; Bovy et al. 2019), but as previously mentioned (see Section 2.2, cut at 5 kpc), we remove all of the stars in the central area for our model. For the outer disk, one would need to add a measurement of the warp, $z_w(R, \phi)$ (e.g., Li et al. 2019), to the stellar distribution. However, since our model is axisymmetric, we cannot add this to our model. In future works, one could investigate whether a shift in z-direction would be a possible parameterization of the warp for an axisymmetric model like ours.

For our modeling, we keep the scale radius of the dark matter halo, r_s, constant at 14.8 kpc (Eilers et al. 2019), since we know that it is not constrained well with our JAM model (Paper I). In addition, 14.8 kpc agrees with the literature values ranging from ∼10–20 kpc. Further, because our data are limited to the disk region, they do not strongly constrain the dark matter axial ratio. Hence, we keep q_{DM} fixed to 1.3 (Posti & Helmi 2019), which they derived using globular clusters. See Appendix B for a model with free q_{DM}.

The standard model has seven free parameters: (i) the inner logarithmic slope of the dark matter halo (α_{DM}), (ii) the dark matter fraction within a sphere with radius $R_\odot$ (f_{DM}), (iii)–(vi) the velocity dispersion ratios or anisotropies (σ_θ/σ_r and σ_ϕ/σ_r) for both the flattest ($q_{\mathrm{MGE}} < 0.2$) Gaussian components (subscript 1) of the MGE and the rest (subscript 2); and (vii) the mass-to-light ratio of the stellar component in the V band $[(M_*/L)_V]$.

The fit to the data is performed using the EMCEE python package of Foreman-Mackey et al. (2013), which implements the affine invariant ensemble sampler for Markov Chain Monte Carlo (MCMC) proposed by Goodman & Weare (2010).

4. Results

4.1. Exponential Disk Model

Using the data and uncertainties described in Section 2, we perform MCMC fits for the Milky Way distribution without flaring as described in Section 3.1.1.

The best-fitting model gives $\chi^2 \sim 9.2$, which is much larger than 1 that we want. This is mainly because there are systematic uncertainties due to nonaxisymmetric features, spiral structure, the equilibrium assumption of JAM, and the choice of the tracer distribution, which our model cannot take into account. This also explains why we get very small statistical errors for our free parameters. The systematic errors would dominate here, and we can use this result to get an estimate of the systematic uncertainties, which are otherwise impossible to determine.

To get more reasonable errors, we check the precision to which our model explains the data. To do this, we quadratically add a value in kilometers per second to our bootstrapped errors,

$$\mathrm{errors}_i^2 = \mathrm{errors}_{\mathrm{bootstr.},i}^2 + \mathrm{errors}_{\mathrm{s.},i}^2, \tag{8}$$

with $\mathrm{errors}_{\mathrm{s.},i}$ such that we get $\chi^2 = 1$ for each component $i = (v_\phi, \sigma_R, \sigma_\phi, \sigma_z)$. The added values for this model are (6.03, 5.01, 6.55, 3.32) km s^{-1}, respectively. With these higher errors for the data, we do a new MCMC fit, and the best-fitting values are listed in the second column ("Model") of Table 1.

However, the statistical uncertainties from the posterior of our best-fitting parameters are only formal errors, which are quite small because of the large number of stars that we use, and systematic uncertainties dominate. To estimate our systematics, we investigate the axisymmetry assumption of our model in Section 4.2, and we give the systematic errors as half of the difference between the minimum and maximum of all of our models with an exponential disk without flaring.

The posterior distribution is shown in Appendix A, Figure 9, and the JAM model is shown in the second column of Figure 5.

[7] We use Python version 6.1.2 of the JAMPY package, available from https://pypi.org/project/jampy/.

Table 1
Best-fitting Parameters

Parameters	Model	Free Anisotropies	Flared Model
$\alpha_{\rm DM}$	$-1.602 \pm 0.015_{\rm stat} \pm 0.079_{\rm syst}$	$-1.592 \pm 0.029_{\rm stat} \pm 0.079_{\rm syst}$	$-1.574 \pm 0.023_{\rm stat}$
$f_{\rm DM}$	$0.811 \pm 0.006_{\rm stat} \pm 0.014_{\rm syst}$	$0.819 \pm 0.013_{\rm stat} \pm 0.014_{\rm syst}$	$0.663 \pm 0.007_{\rm stat}$
$(\sigma_\theta/\sigma_r)_1$	$0.663 \pm 0.006_{\rm stat} \pm 0.021_{\rm syst}$	...	$0.610 \pm 0.0003_{\rm stat}$
$(\sigma_\theta/\sigma_r)_2$	$0.577 \pm 0.011_{\rm stat} \pm 0.038_{\rm syst}$	...	$0.632 \pm 0.003_{\rm stat}$
$(\sigma_\phi/\sigma_r)_1$	$0.711 \pm 0.016_{\rm stat} \pm 0.028_{\rm syst}$	...	$0.848 \pm 0.007_{\rm stat}$
$(\sigma_\phi/\sigma_r)_2$	$1.001 \pm 0.019_{\rm stat} \pm 0.054_{\rm syst}$	...	$0.853 \pm 0.006_{\rm stat}$
$(M_*/L)_V$	$0.413 \pm 0.012_{\rm stat} \pm 0.031_{\rm syst}$	$0.396 \pm 0.028_{\rm stat} \pm 0.031_{\rm syst}$	$0.715 \pm 0.015_{\rm stat}$
$\chi^2_{\rm DOF}$	0.91	0.81	1.3
$v_{\rm circ}(R_\odot)$ [km s^{-1}]	$234.7 \pm 0.3_{\rm stat} \pm 1.7_{\rm syst}$	$234.6 \pm 0.4_{\rm stat} \pm 1.7_{\rm syst}$	$234.6 \pm 0.24_{\rm stat}$
$a_{\rm circ}$ [km s^{-1} kpc^{-1}]	$-1.78 \pm 0.05_{\rm stat} \pm 0.34_{\rm syst}$	$-1.69 \pm 0.08_{\rm stat} \pm 0.34_{\rm syst}$	$-2.39 \pm 0.05_{\rm stat}$

Note. The uncertainties given in this table as statistical errors are derived from the posterior distributions and are the formal errors. For the estimate of the systematic uncertainties, we also use the values from Table 2 in Section 4.2, and we estimate them to be half of the difference between the minimum and maximum of all of our models with an exponential disk without flaring.

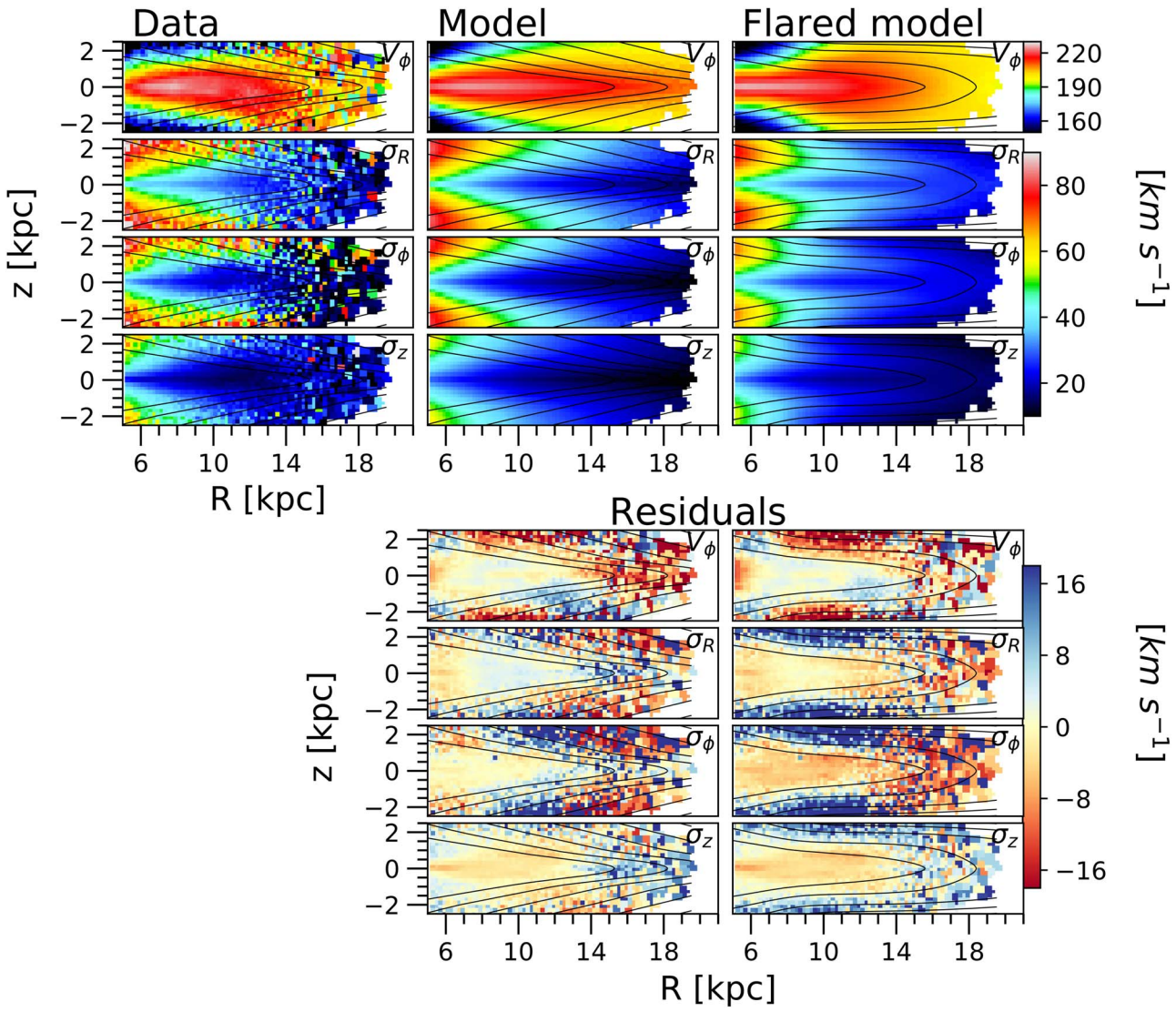

Figure 5. Best fit for JAM$_{\rm sph}$. From left to right, the columns show the data, the JAM model with the Jurić et al. (2008) stellar density distribution, and the JAM model with flaring. At the bottom are the residuals (data-model) for the two JAM models. From top to bottom, the rows show V_ϕ, σ_R, σ_ϕ, and σ_z. The black lines are the stellar density (as described in Section 3.1.1) contours, except for the flared model, which has the contours of the flared disk model described in Section 3.1.2.

The circular velocity is plotted in Figure 6 and has a value of $(234.7 \pm 0.3_{\rm stat} \pm 1.7_{\rm syst})$ km s^{-1} at the solar radius. The slope of the circular velocity curve between 6.2 and 20.2 kpc, which is the region were it can be approximated by a straight line, is declining at $(-1.78 \pm 0.05_{\rm stat} \pm 0.34_{\rm syst})$ km s^{-1} kpc^{-1}. This is consistent with the results of Eilers et al. (2019). A test to

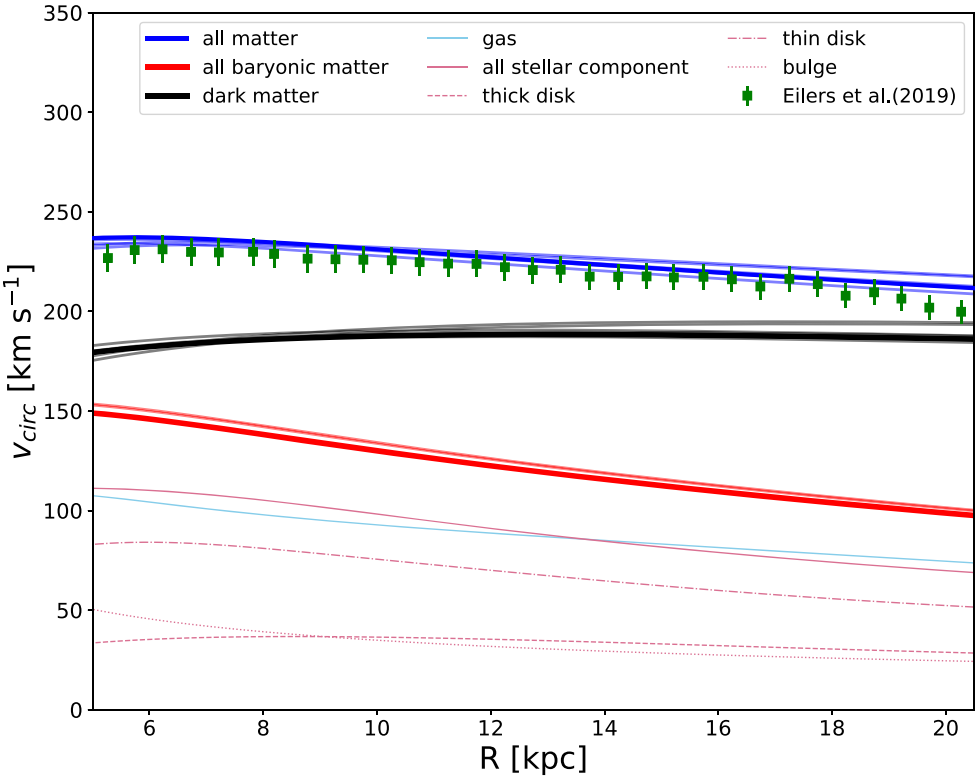

Figure 6. Circular velocity for the JAM_{sph} model without flaring. The blue solid line is our total circular velocity from our best fit, the green squares are the measurements by Eilers et al. (2019) with systematic uncertainties of 3%, the dark matter contribution is shown as a black solid line, and the baryonic contribution is shown as a red solid line. For each of the three lines, there are five fainter lines (close around them), which are the best-fitting results from the four different sectors of the data (Section 4.2) and the model with free anisotropies, and they give an estimate of the systematic uncertainty. Only for the main model without flaring we also have plotted the gas contribution as a light blue line and the total stellar contribution as a light violet solid line, while this can be separated further into the bulge (light violet dotted line), the thin (light violet dashed–dotted line) and thick disk (light violet dashed line). The contribution of the different components plotted here depends on the assumed stellar and dark matter density profiles, and with our model, we only tightly constrain the total circular velocity.

investigate the small offset between our and Eilers et al.'s (2019) measurements of the circular velocity can be found in Appendix C. In Figure 6, we also show the contribution of the different components to the total circular velocity according to our best fit. However, because the covariance of the mass-to-light ratio, the dark matter fraction, and the dark matter slope (see Figure 9), which is expected, the plotted decomposition of the circular velocity into the different components is not the only possible decomposition. One could decrease the dark matter contribution while increasing the stellar component and still get the same total result, which is what we constrain. The smaller than NFW ($\alpha_{\rm DM} = -1$) dark matter slope also increases the dark matter contribution toward smaller radii inside $R_\odot$. This makes the dark matter contribution more dominant for our circular velocity at small radii in comparison to other works (e.g., Eilers et al. 2019, and what we see in Appendix C, Figure 11), where an NFW profile is usually assumed. Hence, we only tightly constrain the total circular velocity and not the different components of it, which depend on the assumed stellar and dark matter density profiles.

One should also note that even though we use giant stars, we do not take the asymmetric drift into account, since we use the full Jeans equations with JAM. The circular velocity is a result of the gravitational potential that we get from our best fit to the individual velocities.

Additionally, for the best-fitting model, the dark matter density at the solar radius is $\rho_{\rm DM}(R_\odot) = (0.00892 \pm 0.00007_{\rm stat} \pm 0.00056_{\rm syst})\ M_\odot\,{\rm pc}^{-3}$, and the total density $\rho_{\rm tot}(R_\odot) = (0.0672 \pm 0.0006_{\rm stat} \pm 0.0015_{\rm syst})\ M_\odot\,{\rm pc}^{-3}$. The total density logarithmic slope in the range of $5\ {\rm kpc} \leqslant R \leqslant 19.5\ {\rm kpc}$ is $\alpha_{\rm tot} = -2.367 \pm 0.007_{\rm stat} \pm 0.047_{\rm syst}$. All statistical errors are the formal errors from the posterior distribution and do not include the systematic uncertainties that would increase the errors.

Comparing these results to our previous work (Paper I), the JAM model agrees with our previous results, and all parameters agree within the respective errors. Specifically, the total densities, in particular on the total slope and dark matter fraction, have smaller uncertainties and are more reliable because we have a longer radial baseline and more data. The discrepancy between the total logarithmic density slope of our best-fitting model and that from Paper I can be explained due to the different radial range probed ($3.5\ {\rm kpc} \leqslant R \leqslant 12.5\ {\rm kpc}$) and the different r_s (20 kpc) assumed for the dark matter halo. If we constrain our slope to a similar range as in Paper I, our value would decrease to roughly $-2.278 \pm 0.007_{\rm stat} \pm 0.047_{\rm syst}$ and get even smaller for a scale radius of 20 kpc. So, in a similar range, our finding for the total density slope is also consistent with that of Paper I.

In addition, we have also calculated the total surface density as a function of radius by analytically integrating the MGE Gaussians. The integral of one Gaussian, between the cylindrical radii R_1 and R_2 and within the height range $|z| < z_{\rm max}$, is given by the following expression:

$$M = (2\pi)^{3/2} \rho_0 q \sigma^3 (e^{-\frac{R_1^2}{2\sigma^2}} - e^{-\frac{R_2^2}{2\sigma^2}}) \,{\rm erf}\left(\frac{z_{\rm max}}{q\sigma\sqrt{2}}\right). \quad (9)$$

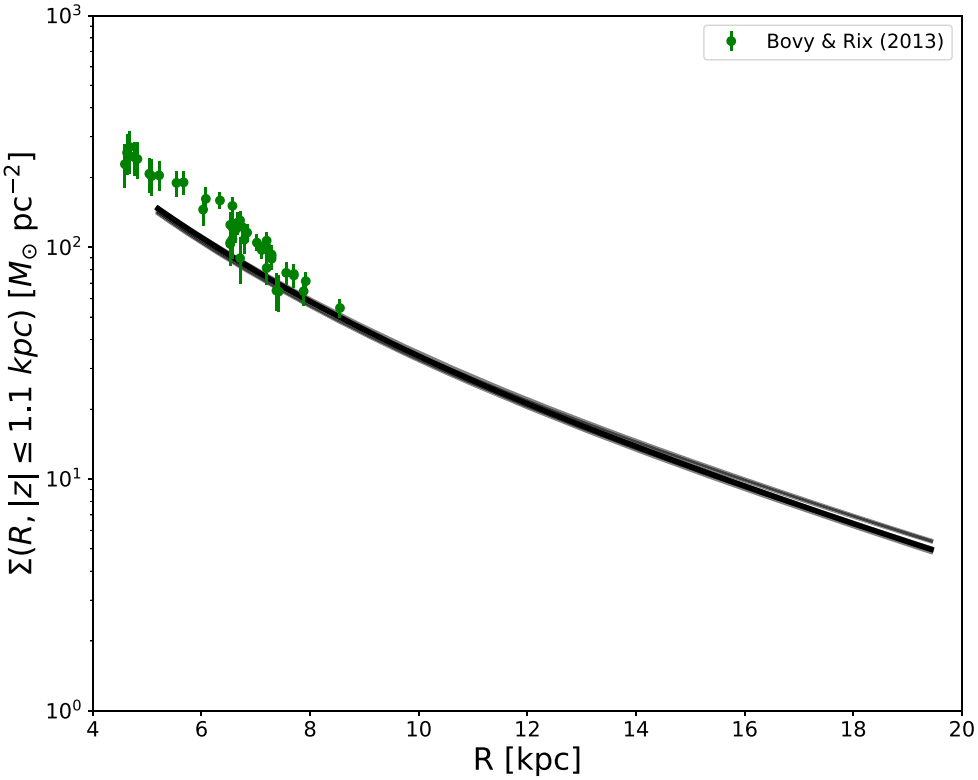

Figure 7. Surface density for the JAM_{sph} model without flaring. The total surface density is calculated in the range -1.1 kpc $\leqslant z \leqslant 1.1$ kpc for our best-fitting model. The green dots are the values from Bovy & Rix (2013), and the five fainter black lines (close around it) are calculated with the best-fitting results from the four different sectors of the data (Section 4.2) and the model with free anisotropies. The radial range (5–19.1 kpc) of the surface density in this plot is between the minimum and maximum radius of the data we used for our best-fitting model (see Figure 5).

This integral was performed for all of the MGE Gaussians for the stellar, gas, and dark matter components for $-1.1\,\mathrm{kpc} \leqslant z \leqslant 1.1\,\mathrm{kpc}$ for direct comparison with Bovy & Rix (2013). The resulting surface density is shown in Figure 7. Our surface density is a little bit lower for radii smaller than $R_\odot$ but agrees within the uncertainties at the solar radius, $\Sigma(R_\odot,\ |z| \leqslant 1.1\,\mathrm{kpc}) = (55.5 \pm 0.5_{\mathrm{stat}} \pm 1.7_{\mathrm{syst}})\ M_\odot\,\mathrm{pc}^{-2}$. Moreover, Piffl et al. (2014) gave $\Sigma(|z| \leqslant 0.9\,\mathrm{kpc}) = (69 \pm 15)\ M_\odot\,\mathrm{pc}^{-2}$ for the solar radius, and our value of $\Sigma(R_\odot,\ |z| \leqslant 0.9\,\mathrm{kpc}) = (51.1 \pm 0.4_{\mathrm{stat}} \pm 1.7_{\mathrm{syst}})\ M_\odot\,\mathrm{pc}^{-2}$ lies within their 3σ range. Since our total surface density also agrees within the uncertainties with previous findings, it gives us another confirmation that our model well constrains the total density, circular velocity, and potential, and only the exact decomposition into the different components (dark matter, stellar, and gas), which is not the scope of this work, is not tightly constrained.

Further, we also performed a fit allowing the 18 Gaussians in the MGE model of the stellar component to have a different anisotropy value, (σ_θ/σ_r) and (σ_ϕ/σ_r). This model has a total of 39 free parameters, and the ones that are not the anisotropies are listed in the column "Free Anisotropies" in Table 1. This model gives a better fit to the data, since it has more parameters, but all "interesting" parameters agree within the 3σ error range with our main model.

4.2. Assessing Systematic Errors Due to Nonaxisymmetries

Our Galaxy contains nonaxisymmetric features due to the Galactic bar (e.g., Monari et al. 2016; Khoperskov et al. 2019), the spiral arms (e.g., Reid et al. 2019; Eilers et al. 2020), the warp of the disk (e.g., Vázquez et al. 2008; Li et al. 2020), or interactions and mergers with satellite galaxies (e.g., Helmi et al. 2018; Koppelman et al. 2019). We now investigate how the model assumption of axisymmetry affects our results by dividing the data set into four sectors, depending on positive or negative z and ϕ: $[z \geqslant 0\,\mathrm{kpc},\ \phi \geqslant 0°]$, $[z \geqslant 0\,\mathrm{kpc},\ \phi < 0°]$, $[z < 0\,\mathrm{kpc},\ \phi \geqslant 0°]$, and $[z < 0\,\mathrm{kpc},\ \phi <]$. If the Milky Way was perfectly axisymmetric, our axisymmetric model should give the same results within the errors for each of the four sectors. Hence, we now fit for each sector separately and compare the different results, in order to estimate how much the nonaxisymmetric features of our Galaxy influence our model and estimate the systematic uncertainties of the free parameters.

For these fits, we use the same errors as for the fit to all data points. The resulting circular velocities are plotted in Figure 6 as fainter and thinner blue lines, and all of the fit parameters are listed in Table 2. The results show us that there are some differences depending on which part of the Galaxy we model; however, most of the free parameters are within the 3σ range of each other and with the total model. Higher discrepancies between the different sectors of the Milky Way exist for α_{DM}, which are outside the 3σ range of the statistical errors.

We can use the discrepancies between the parameters for the different sectors to get an estimate for the systematic uncertainty of our model because of nonaxisymmetric features in the data. The mean values in Table 2 are the mean of the individual sectors, and the errors are half of the differences between the maximum and minimum of the individual sectors. The last column of the table is the total systematic

Table 2
Best-fitting Parameters for the Four Sectors

Parameters	$z \geqslant 0$ kpc, $\phi \geqslant 0°$	$z \geqslant 0$ kpc, $\phi < 0°$	$z < 0$ kpc, $\phi \geqslant 0°$	$z < 0$ kpc, $\phi < 0°$	Mean	Syst. Error
$\alpha_{\rm DM}$	$-1.623 \pm 0.017_{\rm stat}$	$-1.627 \pm 0.018_{\rm stat}$	$-1.469 \pm 0.019_{\rm stat}$	$-1.487 \pm 0.019_{\rm stat}$	-1.552 ± 0.079	± 0.079
$f_{\rm DM}$	$0.837 \pm 0.007_{\rm stat}$	$0.830 \pm 0.008_{\rm stat}$	$0.816 \pm 0.007_{\rm stat}$	$0.838 \pm 0.007_{\rm stat}$	0.830 ± 0.011	± 0.014
$(\sigma_\theta/\sigma_r)_1$	$0.653 \pm 0.006_{\rm stat}$	$0.655 \pm 0.008_{\rm stat}$	$0.666 \pm 0.008_{\rm stat}$	$0.709 \pm 0.010_{\rm stat}$	0.671 ± 0.021	± 0.021
$(\sigma_\theta/\sigma_r)_2$	$0.569 \pm 0.011_{\rm stat}$	$0.610 \pm 0.014_{\rm stat}$	$0.601 \pm 0.013_{\rm stat}$	$0.568 \pm 0.014_{\rm stat}$	0.587 ± 0.038	± 0.038
$(\sigma_\phi/\sigma_r)_1$	$0.695 \pm 0.017_{\rm stat}$	$0.702 \pm 0.017_{\rm stat}$	$0.702 \pm 0.018_{\rm stat}$	$0.771 \pm 0.019_{\rm stat}$	0.718 ± 0.028	± 0.028
$(\sigma_\phi/\sigma_r)_2$	$0.911 \pm 0.021_{\rm stat}$	$0.983 \pm 0.024_{\rm stat}$	$0.940 \pm 0.023_{\rm stat}$	$0.894 \pm 0.024_{\rm stat}$	0.932 ± 0.045	± 0.054
$(M_*/L)_V$	$0.355 \pm 0.015_{\rm stat}$	$0.361 \pm 0.016_{\rm stat}$	$0.401 \pm 0.015_{\rm stat}$	$0.352 \pm 0.015_{\rm stat}$	0.367 ± 0.025	± 0.031
$\chi^2_{\rm DOF}$	0.98	0.97	1.03	1.05	...	...
$v_{\rm circ}(R_\odot)$ [km s^{-1}]	$233.7 \pm 0.3_{\rm stat}$	$231.4 \pm 0.3_{\rm stat}$	$234.3 \pm 0.3_{\rm stat}$	$232.9 \pm 0.3_{\rm stat}$	233.1 ± 1.5	± 1.7
$a_{\rm vcirc}$ [km s^{-1} kpc^{-1}]	$-1.71 \pm 0.06_{\rm stat}$	$-1.76 \pm 0.07_{\rm stat}$	$-1.18 \pm 0.07_{\rm stat}$	$-1.11 \pm 0.06_{\rm stat}$	-1.44 ± 0.33	± 0.34

Note. The uncertainties given in this table as statistical errors are derived from the posterior distributions and are the formal errors. The estimates of the systematic uncertainties, given in the last column, are the same as in Table 1. In addition, we give the mean value of the four sectors and its error, which is half of the difference of the minimum and maximum of the individual sectors (error = (max − min)/2).

errors = (max − min)/2, including the best-fitting values from Table 1 without flaring and the model with free anisotropies. These systematic errors from the sectors and from all of our models without flaring might be the same if the minimum and maximum values are from the four sectors.

Additionally, for the four sectors, the mean dark matter density at the solar radius is $\rho_{\rm DM}(R_\odot) = (0.00935 \pm 0.00056_{\rm syst})\ M_\odot\,{\rm pc}^{-3}$, and the mean total density $\rho_{\rm tot}(R_\odot) = (0.0654 \pm 0.0015_{\rm syst})\ M_\odot\,{\rm pc}^{-3}$. The mean total density logarithmic slope $\alpha_{\rm tot} = -2.322 \pm 0.047_{\rm syst}$ for 5 kpc $\leqslant R \leqslant$ 19.5 kpc, and the mean local surface density $\Sigma(R_\odot,\ |z| \leqslant 1.1\ {\rm kpc}) = (54.6 \pm 1.7_{\rm syst})\ M_\odot\,{\rm pc}^{-2}$. All of the errors given here are the same systematic errors as in Section 4.1 using the four sectors, the best-fitting model, and the model with free anisotropies.

4.3. Flared Disk Model

In Section 3.1.2, we also explained how we can change our stellar distribution to account for the flaring of the disk. Using this distribution, we test how that affects our model.

We use the same errors as before, and the fit results are listed in Table 1 with their formal errors. The model result is shown in the third column of Figure 5, and the posterior distribution is shown in Appendix A, Figure 10. From the posterior distribution and the table, one can notice that the statistical uncertainty of $(\sigma_\theta/\sigma_r)_1$ is an order of magnitude smaller than for the rest of the velocity dispersion ratios, even though the fit has converged properly. This confirms that the formal errors are not reliable, since they are too small and the systematic uncertainties of the model would dominate.

Further, the dark matter density at the solar radius $\rho_{\rm DM}(R_\odot) = (0.00715 \pm 0.00007_{\rm stat})\ M_\odot\,{\rm pc}^{-3}$, and the total density $\rho_{\rm tot}(R_\odot) = (0.08561 \pm 0.00073_{\rm stat})\ M_\odot\,{\rm pc}^{-3}$. The total density logarithmic slope $\alpha_{\rm tot} = -2.451 \pm 0.010_{\rm stat}$ for 5 kpc $\leqslant R \leqslant$ 19.5 kpc, and the local surface density $\Sigma(R_\odot,\ |z| \leqslant 1.1\ {\rm kpc}) = (64.1 \pm 0.6_{\rm stat})\ M_\odot\,{\rm pc}^{-2}$.

From the χ^2 value, one can see that the fit with flaring is not as good as without it, which could be due to our choice of flare parameters. Also, if we compare the residuals of the two models, one can notice that the residuals get higher away from the midplane for the model with flaring. On the other hand, around the midplane, it seems to be similarly good or only slightly higher than the model without the flaring. The differences between the models with and without flaring can also be seen in Figure 8.

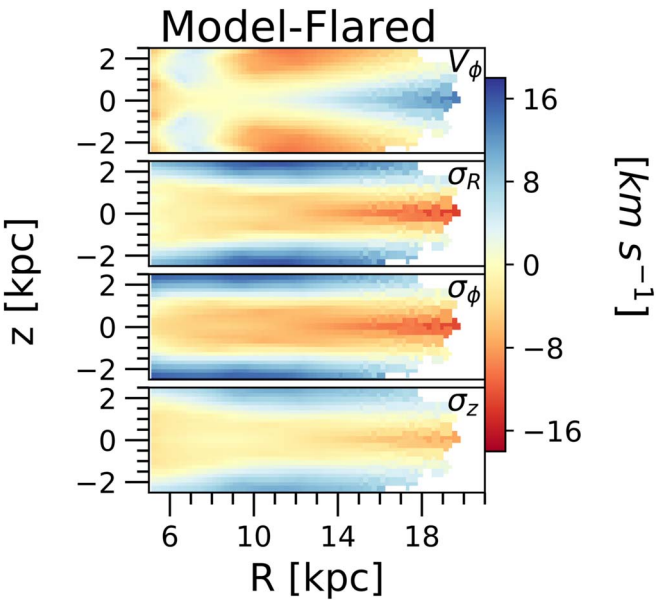

Figure 8. Difference between the JAM$_{\rm sph}$ without and with a flared disk. From top to bottom, the rows show V_ϕ, σ_R, σ_ϕ, and σ_z.

We do not have systematic uncertainties because the investigation in the previous section was with a different Milky Way model without flaring, and the flared model does not fit the data as well; thus, we cannot assume that they have the same systematics, and further study would be needed. As mentioned above, the flared model might give a slightly worse fit to our data only because of the flare parameters we selected, since we just added a parameterization of the scale height, $h(z)$, to our normal model without flaring. Additionally, to fully test if the flared model provides a better fit to the data, one would need to do a detailed study of the flare and test which parameterization for the scale heights is the best for the Milky Way disk. This is beyond the scope of this paper, and we just want to get a first idea of how our model changes if we include a flare.

5. Conclusion

In this paper, we construct a dynamical Jeans model of the Milky Way disk using the $\mathrm{JAM_{sph}}$ code (Cappellari 2020).

The data we use are based on Gaia EDR3, combined with the Hogg et al. (2019) data set, which is combined APOGEE, Gaia DR2, 2MASS, and WISE data with precise spectrophotometric distance estimates. The combined data set enlarges the range of galactocentric distances that we cover. We probe an area in the range of $5.0\ \mathrm{kpc} \leqslant R \leqslant 19.5\ \mathrm{kpc}$ and $-2.5\ \mathrm{kpc} \leqslant z \leqslant 2.5\ \mathrm{kpc}$.

Our main results are consistent with Paper I within the uncertainties but more reliable because of the more extended radial range of our data.

The best-fit value for the dark matter slope is $\alpha_{\mathrm{DM}} = -1.602 \pm 0.015_{\mathrm{stat}} \pm 0.079_{\mathrm{syst}}$, which is smaller than –1 (NFW), and the dark matter density at the solar radius is $(0.00892 \pm 0.00007_{\mathrm{stat}} \pm 0.00056_{\mathrm{syst}})\ M_{\odot}\ \mathrm{pc}^{-3}$. These values agree with our previous work (Paper I) and are consistent with other works for the dark matter slope, which indicate that a steeper slope than NFW is needed for the disk region (Portail et al. 2017; Cole & Binney 2017). The dark matter density at the solar position is slightly smaller than in previous works (McKee et al. 2015; McMillan 2017; Paper I), which might be because we constrain the total density and the decomposition is more uncertain, similar to what we explained for the circular velocity. However, the values still agree in the 3σ range of the uncertainties. The circular velocity at the solar position is $(234.7 \pm 0.3_{\mathrm{stat}} \pm 1.7_{\mathrm{syst}})\ \mathrm{km\ s}^{-1}$ with a mild decline toward larger radii of $a_{\mathrm{circ}} = (-1.78 \pm 0.05_{\mathrm{stat}} \pm 0.34_{\mathrm{syst}})\ \mathrm{km\ s}^{-1}\ \mathrm{kpc}^{-1}$, which is consistent with the results from Eilers et al. (2019). The total density at the solar radius is $\rho_{\mathrm{tot}}(R_{\odot}) = (0.0672 \pm 0.0006_{\mathrm{stat}} \pm 0.0015_{\mathrm{syst}})\ M_{\odot}\ \mathrm{pc}^{-3}$, and the total density logarithmic slope is $\alpha_{\mathrm{tot}} = -2.367 \pm 0.007_{\mathrm{stat}} \pm 0.047_{\mathrm{syst}}$ for $5\ \mathrm{kpc} \leqslant R \leqslant 19.5\ \mathrm{kpc}$. All of these values are consistent our previous work (Paper I) within the errors and $-2.278 \pm 0.007 \pm 0.047_{\mathrm{syst}}$ for $3.5 \leqslant R \leqslant 12.5\ \mathrm{kpc}$ (as in Paper I). The total density slope is also consistent with the slope inferred from early-type disk galaxies (Cappellari et al. 2015), and the total solar density is again smaller compared to other works but agrees within the 3σ uncertainties of the work by McKee et al. (2015). Further, the local surface density is $\Sigma(R_{\odot},\ |z| \leqslant 1.1\ \mathrm{kpc}) = (55.5 \pm 0.5_{\mathrm{stat}} \pm 1.7_{\mathrm{syst}})\ M_{\odot}\ \mathrm{pc}^{-2}$, which is slightly lower than other findings (e.g., Bovy & Rix 2013; Piffl et al. 2014) but still within the uncertainties.

Additionally, we also test how the nonaxisymmetries of the gravitational potential change our result.

We further investigate how a flared disk changes our results. It provides a similarly good fit, but in the future, one could perform a more thorough analysis of the parameter space to better constrain the flaring of the disk given its dynamical properties.

The regions that are not included in our model are the bar in the inner part and the warp in the outer disk. These features are nonaxisymmetric, and we cannot reproduce them with our model. We avoid the bar influence by excluding the region inside 5 kpc, but the warp is still affecting our model. Hence, one should note that the regions of our data strongly influenced by this feature (the outer disk) are not well reproduced with our model due to the axisymmetry assumption.

The kinematics used in this paper and the MGE components can be found in the file in the online version. The kinematic data can be used to recreate Figures 1 and 2 and the best-fitting results of Table 1, while the kinematics of the individual sectors were used to get the best-fitting parameters of Table 2. The MGE data sets are useful for Figures 1, 2, and 5 and described in Section 3. The full details are available in the package.

We thank David W. Hogg for his helpful advice and input regarding this project. We thank the anonymous referee for a constructive report that helped to improve the paper.

This work has made use of data from the European Space Agency (ESA) mission Gaia (https://www.cosmos.esa.int/gaia), processed by the Gaia Data Processing and Analysis Consortium (DPAC; https://www.cosmos.esa.int/web/gaia/dpac/consortium). Funding for the DPAC has been provided by national institutions, in particular the institutions participating in the Gaia Multilateral Agreement.

N.N. gratefully acknowledges support by the Deutsche Forschungsgemeinschaft (DFG, German Research Foundation)—Project-ID 138713538—SFB 881 ("The Milky Way System", subproject B8).

A.C.E. acknowledges support by NASA through NASA Hubble Fellowship grant No. HF2-51434 awarded by the Space Telescope Science Institute, which is operated by the Association of Universities for Research in Astronomy, Inc., for NASA, under contract NAS5-26555.

Appendix A
Posterior Distribution

The posterior distribution of the the best-fitting model without flaring (see Section 4.1) is shown in Figure 9. Additionally, Figure 10 shows the posterior distribution for the best-fitting model with a flared disk (see Section 4.3). We have also tested how the result changes with $\mathrm{JAM_{cyl}}$ (Cappellari 2008) for the flared model, and we see that the results are almost the same. The only difference is that the small formal errors of $(\sigma_{\theta}/\sigma_{r})_{1}$ are getting of the same order as the other ratios and that χ^2_{DOF} is slightly smaller ($\chi^2_{\mathrm{DOF}} = 1.07$), which can be a coincidence, since the flared model we use might be wrong, and the cylindrical alignment may happen to compensate for that.

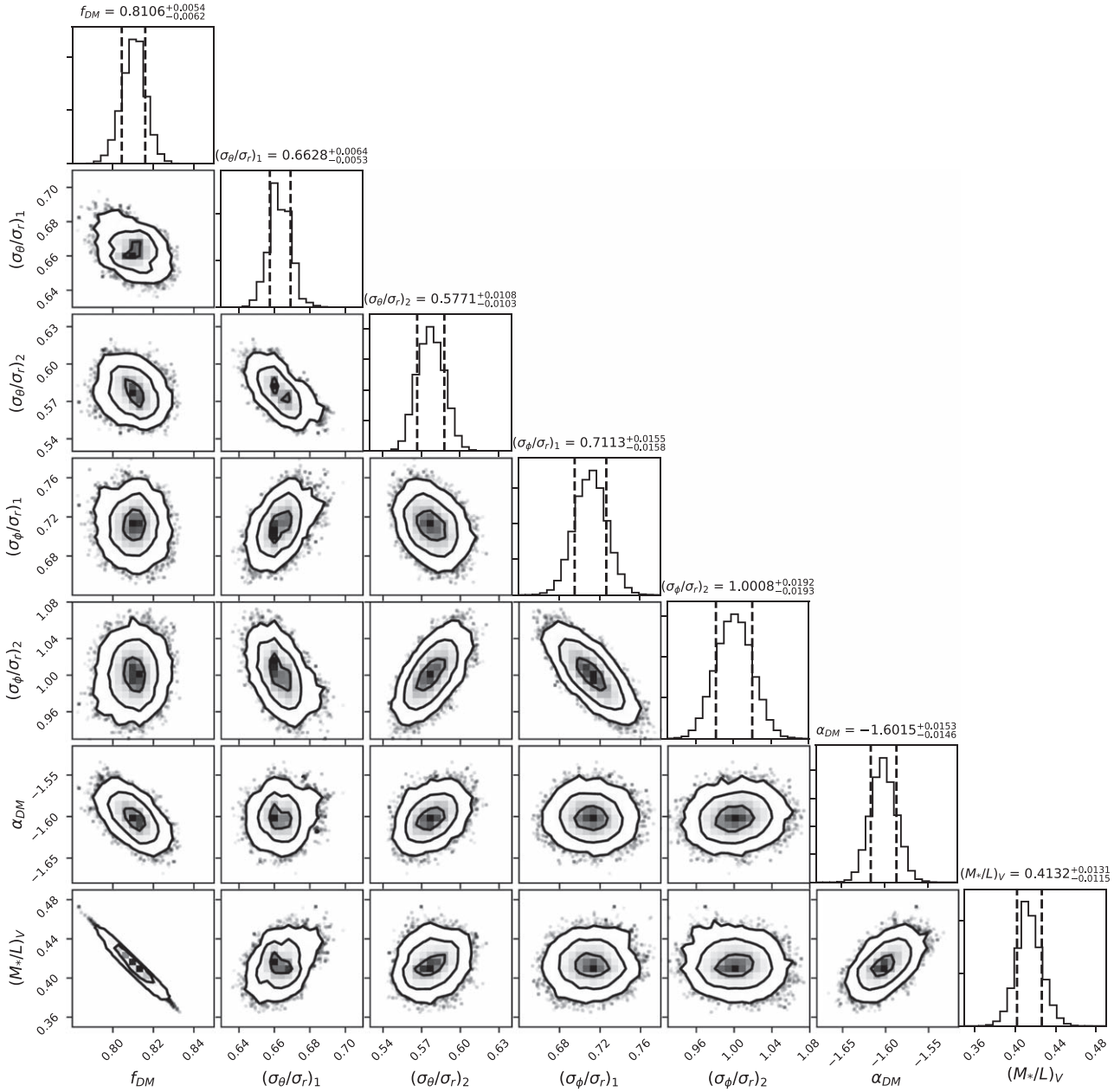

Figure 9. Posterior distribution for the best-fitting JAM_{sph} with an exponential disk model. This is the corner plot for the fit without a flared disk (see Section 4.1). The panels show posterior probability distributions marginalized over two dimensions (contours) and one dimension (histograms). The thick contours represent the 1σ, 2σ, and 3σ confidence levels for one degree of freedom. The numbers with errors on top of each plot are the median and 16th and 84th percentiles of the posterior for each parameter (black dashed lines).

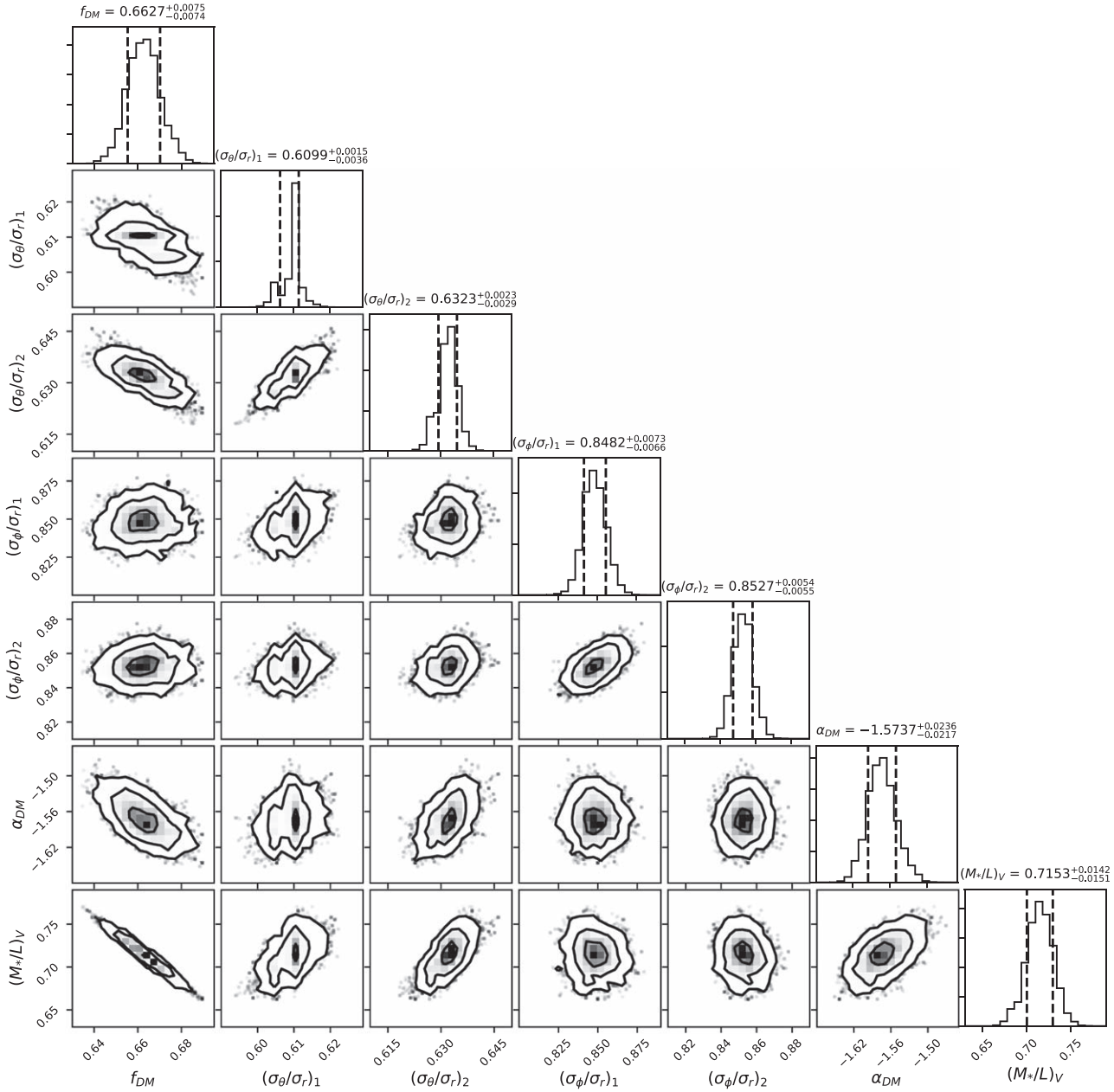

Figure 10. Posterior distribution for the best-fitting $\mathrm{JAM_{sph}}$ with a flared disk model. This is the corner plot for the fit with a flared disk (see Section 4.3). The panels show posterior probability distributions marginalized over two dimensions (contours) and one dimension (histograms). The thick contours represent the 1σ, 2σ, and 3σ confidence levels for one degree of freedom. The numbers with errors on top of each plot are the median and 16th and 84th percentiles of the posterior for each parameter (black dashed lines).

Appendix B
The Dark Matter Axial Ratio (q_{DM}) as a Free Parameter

For our main model, we have fixed $q_{\mathrm{DM}} = 1.3$ (Posti & Helmi 2019); here we show a model if we allow q_{DM} to be free. The resulting free parameters with a free q_{DM} for a model without flaring are listed in Table 3.

What we also see from the posterior distribution is that q_{DM} tends to get high values and has a correlation with the mass-to-light

Table 3
Best-fitting Parameters for the Model with $q_{\rm DM}$ Free

Parameters	$q_{\rm DM}$ Free
$\alpha_{\rm DM}$	$-1.576 \pm 0.026_{\rm stat}$
$f_{\rm DM}$	$0.788 \pm 0.009_{\rm stat}$
$(\sigma_\theta/\sigma_r)_1$	0.664 ± 0.007
$(\sigma_\theta/\sigma_r)_2$	$0.572 \pm 0.010_{\rm stat}$
$(\sigma_\phi/\sigma_r)_1$	$0.707 \pm 0.016_{\rm stat}$
$(\sigma_\phi/\sigma_r)_2$	$1.004 \pm 0.021_{\rm stat}$
$(M_*/L)_V$	$0.480 \pm 0.026_{\rm stat}$
$\chi^2_{\rm DOF}$	0.906
$q_{\rm DM}$	$1.473 \pm 0.068_{\rm stat}$
$v_{\rm circ}(R_\odot)$ [km s^{-1}]	$235.21 \pm 0.27_{\rm stat}$
$a_{\rm vcirc}$ [km s^{-1} kpc^{-1}]	$-1.83 \pm 0.05_{\rm stat}$

Note. All uncertainties given in this table are statistical errors derived from the posterior distributions.

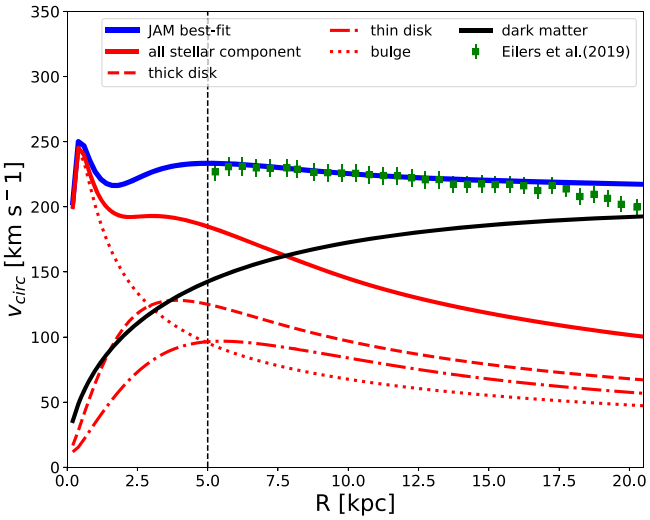

Figure 11. Circular velocity curve with the same assumptions for the tracer distribution and the data as in Eilers et al. (2019). The green squares are the measurements from Eilers et al. (2019) with 3% systematic errors. Our circular velocity curve using the potential we get using JAM is shown in blue, and the stellar component is shown as a red solid line, while the thin disk is a red dashed–dotted line, the thick disk is a dashed line, and the bulge is a dotted line. The dark matter halo is shown as a black solid line. The inner part of the galaxy, i.e., $R < 5$ kpc (indicated by the black vertical dashed line at $R = 5$ kpc), was excluded from the analysis by Eilers et al. (2019) due to the nonaxisymmetric influence of the Galactic bar.

ratio $[(M_*/L)_V]$. Since a too-high $q_{\rm DM}$ value is nonphysical, we keep it fixed for our models in the main text.

Appendix C
Investigating the Offset of $V_{\rm circ}$ between Our Result and Previous Work

Additionally, we have investigated the offset we found between the circular velocity from Eilers et al. (2019) and ours. We had already seen an offset in the previous calculation with the best-fitting JAM model in Paper I.

To do that, we assume the same Milky Way model as in Eilers et al. (2019). We adopt a spherical NFW profile (Navarro et al. 1996); for the thin and thick disks, we assume Miyamoto–Nagai profiles (Miyamoto & Nagai 1975); and for the bulge, we assume a spherical Plummer potential (Plummer 1911), while adapting the parameter values of Pouliasis et al. (2017, model I). Furthermore, we use only the Hogg et al. (2019) data that satisfy $|z| < 0.5$ kpc or $\tan(z/R) < 6^\circ$ and have more than three stars in each 200 pc × 200 pc bin. Finally, we assume $R_\odot = 8.122$ kpc (Gravity Collaboration et al. 2018), $z_\odot = 0.025$ kpc (Jurić et al. 2008), and, as solar velocities in cylindrical Galactic coordinates, $(U_\odot, V_\odot, W_\odot) = (-11.1, 245.8, 7.8)$ km s^{-1} (Reid & Brunthaler 2004).

Using JAM$_{\rm cyl}$ (Cappellari 2008) and the above assumptions, we can almost perfectly reproduce the velocity curve by Eilers et al. (2019); see Figure 11, which is plotted as Figure 3 in Eilers et al. (2019), for comparison.

This proves that the offset we have in our main model is not caused by the modeling method but rather by the data set and the Galaxy model we assume. Small discrepancies are toward the center, where we do not have data, and toward higher radii. The last one confirms our suspicion that the Pouliasis et al. (2017) model overestimates the mass in the inner parts and therefore underestimates the stellar mass toward larger radii to compensate for it, which causes a high dark matter mass at larger radii.

ORCID iDs

Maria Selina Nitschai https://orcid.org/0000-0002-2941-4480
Anna-Christina Eilers https://orcid.org/0000-0003-2895-6218
Nadine Neumayer https://orcid.org/0000-0002-6922-2598
Michele Cappellari https://orcid.org/0000-0002-1283-8420
Hans-Walter Rix https://orcid.org/0000-0003-4996-9069

References

Abolfathi, B., Aguado, D. S., Aguilar, G., et al. 2018, ApJS, 235, 42
Alard, C. 2000, arXiv:astro-ph/0007013
Allende Prieto, C., Majewski, S. R., Schiavon, R., et al. 2008, AN, 329, 1018
Anders, F., Khalatyan, A., Chiappini, C., et al. 2019, A&A, 628, A94
Antoja, T., Helmi, A., Romero-Gómez, M., et al. 2018, Natur, 561, 360
Bacon, R. 1985, A&A, 143, 84
Bacon, R., Simien, F., & Monnet, G. 1983, A&A, 128, 405
Bailer-Jones, C. A. L., Rybizki, J., Fouesneau, M., Demleitner, M., & Andrae, R. 2021, AJ, 161, 147
Binney, J. 2012, MNRAS, 426, 1328
Binney, J., & McMillan, P. 2011, MNRAS, 413, 1889
Binney, J., & Tremaine, S. 1987, Galactic dynamics (Princeton, NJ: Princeton Univ Press)
Bissantz, N., & Gerhard, O. 2002, MNRAS, 330, 591
Bland-Hawthorn, J., & Gerhard, O. 2016, ARA&A, 54, 529
Boubert, D., & Everall, A. 2020, MNRAS, 497, 4246
Boubert, D., Everall, A., & Holl, B. 2020, MNRAS, 497, 1826
Bovy, J., Leung, H. W., Hunt, J. A. S., et al. 2019, MNRAS, 490, 4740
Bovy, J., Nidever, D. L., Rix, H.-W., et al. 2014, ApJ, 790, 127
Bovy, J., & Rix, H.-W. 2013, ApJ, 779, 115
Bovy, J., & Tremaine, S. 2012, ApJ, 756, 89
Cappellari, M. 2002, MNRAS, 333, 400
Cappellari, M. 2008, MNRAS, 390, 71
Cappellari, M. 2016, ARA&A, 54, 597
Cappellari, M. 2020, MNRAS, 494, 4819
Cappellari, M., Bacon, R., Bureau, M., et al. 2006, MNRAS, 366, 1126
Cappellari, M., & Copin, Y. 2003, MNRAS, 342, 345
Cappellari, M., Romanowsky, A. J., Brodie, J. P., et al. 2015, ApJL, 804, L21
Cappellari, M., Scott, N., Alatalo, K., et al. 2013, MNRAS, 432, 1709
Cole, D. R., & Binney, J. 2017, MNRAS, 465, 798
de Lorenzi, F., Gerhard, O., Coccato, L., et al. 2009, MNRAS, 395, 76
Dehnen, W. 2009, MNRAS, 395, 1079
Efron, B., & Tibshirani, R. 1993, An Introduction to the Bootstrap (London: Chapman and Hall/CRC)
Eilers, A.-C., Hogg, D. W., Rix, H.-W., et al. 2020, ApJ, 900, 186
Eilers, A.-C., Hogg, D. W., Rix, H.-W., & Ness, M. K. 2019, ApJ, 871, 120

Emsellem, E., Monnet, G., & Bacon, R. 1994, A&A, 285, 723
Everall, A., Evans, N. W., Belokurov, V., & Schönrich, R. 2019, MNRAS, 489, 910
Flynn, C., Holmberg, J., Portinari, L., Fuchs, B., & Jahreiß, H. 2006, MNRAS, 372, 1149
Foreman-Mackey, D., Hogg, D. W., Lang, D., & Goodman, J. 2013, PASP, 125, 306
Gaia Collaboration, Brown, A. G. A., Vallenari, A., et al. 2018b, A&A, 616, A1
Gaia Collaboration, Brown, A. G. A., Vallenari, A., et al. 2021, A&A, 649, A1
Gaia Collaboration, Katz, D., Antoja, T., et al. 2018a, A&A, 616, A11
Gaia Collaboration, Prusti, T., de Bruijne, J. H. J., et al. 2016, A&A, 595, A1
Gebhardt, K., Richstone, D., Kormendy, J., et al. 2000, AJ, 119, 1157
Goodman, J., & Weare, J. 2010, Communications in Applied Mathematics and Computational Science, 5, 65
Grabelsky, D. A., Cohen, R. S., Bronfman, L., Thaddeus, P., & May, J. 1987, ApJ, 315, 122
Gravity Collaboration, Abuter, R., Amorim, A., et al. 2018, A&A, 615, L15
Gravity Collaboration, Abuter, R., Amorim, A., et al. 2019, A&A, 625, L10
Gyuk, G., Flynn, C., & Evans, N. W. 1999, ApJ, 521, 190
Hagen, J. H. J., Helmi, A., de Zeeuw, P. T., & Posti, L. 2019, A&A, 629, A70
Helmi, A., Babusiaux, C., Koppelman, H. H., et al. 2018, Natur, 563, 85
Hogg, D. W., Eilers, A.-C., & Rix, H.-W. 2019, AJ, 158, 147
Jeans, J. H. 1915, MNRAS, 76, 70
Jeans, J. H. 1922, MNRAS, 82, 122
Jin, Y., Zhu, L., Long, R. J., et al. 2019, MNRAS, 486, 4753
Joshi, Y. C. 2007, MNRAS, 378, 768
Jurić, M., Ivezić, Ž, Brooks, A., et al. 2008, ApJ, 673, 864
Kerr, F. J. 1957, AJ, 62, 93
Khoperskov, S., Di Matteo, P., Gerhard, O., et al. 2019, A&A, 622, L6
Koppelman, H. H., Helmi, A., Massari, D., Price-Whelan, A. M., & Starkenburg, T. K. 2019, A&A, 631, L9
Lablanche, P.-Y., Cappellari, M., Emsellem, E., et al. 2012, MNRAS, 424, 1495
Leung, G. Y. C., Leaman, R., van de Ven, G., et al. 2018, MNRAS, 477, 254
Li, C., Zhao, G., Jia, Y., et al. 2019, ApJ, 871, 208
Li, H., Li, R., Mao, S., et al. 2016, MNRAS, 455, 3680
Li, X. Y., Huang, Y., Chen, B. Q., et al. 2020, ApJ, 901, 56
Lindegren, L., Bastian, U., Biermann, M., et al. 2021b, A&A, 649, A4
Lindegren, L., Hernández, J., Bombrun, A., et al. 2018, A&A, 616, A2
Lindegren, L., Klioner, S. A., Hernández, J., et al. 2021a, A&A, 649, A2
Liu, C., Xu, Y., Wan, J.-C., et al. 2017, RAA, 17, 096
López-Corredoira, M., Cabrera-Lavers, A., Garzón, F., & Hammersley, P. L. 2002, A&A, 394, 883
López-Corredoira, M., & Molgó, J. 2014, A&A, 567, A106
Mackereth, J. T., & Bovy, J. 2020, MNRAS, 492, 3631
Majewski, S. R., Schiavon, R. P., Frinchaboy, P. M., et al. 2017, AJ, 154, 94
May, J., Alvarez, H., & Bronfman, L. 1997, A&A, 327, 325
McKee, C. F., Parravano, A., & Hollenbach, D. J. 2015, ApJ, 814, 13
McMillan, P. J. 2017, MNRAS, 465, 76
Miyamoto, M., & Nagai, R. 1975, PASJ, 27, 533
Momany, Y., Zaggia, S., Gilmore, G., et al. 2006, A&A, 451, 515
Monari, G., Famaey, B., Siebert, A., et al. 2016, MNRAS, 461, 3835
Navarro, J. F., Frenk, C. S., & White, S. D. M. 1996, ApJ, 462, 563
Nitschai, M. S., Cappellari, M., & Neumayer, N. 2020, MNRAS, 494, 6001
Oort, J. H., Kerr, F. J., & Westerhout, G. 1958, MNRAS, 118, 379
Piffl, T., Binney, J., McMillan, P. J., et al. 2014, MNRAS, 445, 3133
Plummer, H. C. 1911, MNRAS, 71, 460
Portail, M., Gerhard, O., Wegg, C., & Ness, M. 2017, MNRAS, 465, 1621
Posti, L., & Helmi, A. 2019, A&A, 621, A56
Pouliasis, E., Di Matteo, P., & Haywood, M. 2017, A&A, 598, A66
Reid, M. J., & Brunthaler, A. 2004, ApJ, 616, 872
Reid, M. J., Menten, K. M., Brunthaler, A., et al. 2019, ApJ, 885, 131
Reid, M. J., Menten, K. M., Zheng, X. W., et al. 2009, ApJ, 700, 137
Reylé, C., Marshall, D. J., Robin, A. C., & Schultheis, M. 2009, A&A, 495, 819
Rix, H.-W., & Bovy, J. 2013, A&ARv, 21, 61
Rix, H.-W., de Zeeuw, P. T., Cretton, N., van der Marel, R. P., & Carollo, C. M. 1997, ApJ, 488, 702
Rybizki, J., Rix, H.-W., Demleitner, M., Bailer-Jones, C. A. L., & Cooper, W. J. 2021, MNRAS, 500, 397
Schönrich, R., Binney, J., & Dehnen, W. 2010, MNRAS, 403, 1829
Schönrich, R., McMillan, P., & Eyer, L. 2019, MNRAS, 487, 3568
Schwarzschild, M. 1979, ApJ, 232, 236
Skowron, D. M., Skowron, J., Mróz, P., et al. 2019, AcA, 69, 305
Skrutskie, M. F., Cutri, R. M., Stiening, R., et al. 2006, AJ, 131, 1163
Syer, D., & Tremaine, S. 1996, MNRAS, 282, 223
Torra, F., Castañeda, J., Fabricius, C., et al. 2021, A&A, 649, A10
van de Ven, G., van den Bosch, R. C. E., Verolme, E. K., & de Zeeuw, P. T. 2006, A&A, 445, 513
van den Bosch, R. C. E., van de Ven, G., Verolme, E. K., Cappellari, M., & de Zeeuw, P. T. 2008, MNRAS, 385, 647
van der Marel, R. P., Cretton, N., de Zeeuw, P. T., & Rix, H.-W. 1998, ApJ, 493, 613
Vázquez, R. A., May, J., Carraro, G., et al. 2008, ApJ, 672, 930
Vogelsberger, M., Genel, S., Springel, V., et al. 2014, Natur, 509, 177
Watkins, L. L., van der Marel, R. P., Bellini, A., & Anderson, J. 2015, ApJ, 812, 149
Wegg, C., Gerhard, O., & Bieth, M. 2019, MNRAS, 485, 3296
Wegg, C., Gerhard, O., & Portail, M. 2015, MNRAS, 450, 4050
Widrow, L. M., Gardner, S., Yanny, B., Dodelson, S., & Chen, H.-Y. 2012, ApJL, 750, L41
Wright, E. L., Eisenhardt, P. R. M., Mainzer, A. K., et al. 2010, AJ, 140, 1868
Wyithe, J. S. B., Turner, E. L., & Spergel, D. N. 2001, ApJ, 555, 504
Yusifov, I. 2004, in The Magnetized Interstellar Medium, ed. B. Uyaniker, W. Reich, & R. Wielebinski (Katlenburg-Lindau: Copernicus GmbH), 165
Zhang, L., Rix, H.-W., van de Ven, G., et al. 2013, ApJ, 772, 108
Zinn, J. C., Pinsonneault, M. H., Huber, D., & Stello, D. 2019, ApJ, 878, 136